Journal of Nonlinear Science (2023) 33:81
https://doi.org/10.1007/s00332-023-09936-8

Journal of Nonlinear Science

The Impact of Frequency Bandwidth on a One-Dimensional Model for Dispersive Wave Turbulence

Ryan Shìjié Dù[1] · Oliver Bühler[1]

Received: 28 November 2022 / Accepted: 8 June 2023

Abstract

We combine theory and high-resolution direct numerical simulation to resolve a long-standing puzzle concerning the forced–dissipative statistics of a one-dimensional model for dispersive wave turbulence, which was introduced by Majda et al. (J Nonlinear Sci 6:9–44, 1997. https://doi.org/10.1007/BF02679124) as a test bed for wave turbulence theory (WTT). Numerous earlier studies had indicated significant discrepancies between the inertial range power law predictions of WTT and those observed in direct numerical simulations of that model. Exactly why and when these discrepancies would arise had been an open question. On the theoretical side, we utilize an exact scaling symmetry of the model to derive a one-parameter family of exact self-similar power laws for the inertial range, which includes the WTT prediction as a special case. We follow this up by numerical simulations at unprecedented resolution, combining white-noise forcing, infrared and ultraviolet dissipation, and a novel averaging technique for the estimation of mean values. Our converged numerical results refute an earlier hypothesis that the discrepancies might be due to variations in wave amplitude. Instead, we find incontrovertible evidence that the WTT prediction is always achieved across a wide range of wave amplitudes, but only if the inertial range is wide enough when measured in the ratio of wave frequency at the forcing scales to wave frequency at the dissipation scales. For a concave dispersion relation (as for deep water waves), frequency bandwidth is a much more stringent criterion than wavenumber bandwidth. At finite resolution, the observed power law is always steeper than the WTT prediction, but to excellent approximation the discrepancy in the exponent is simply proportional to the aforementioned frequency ratio. The picture that emerges is that of a self-similar WTT inertial range that is robustly 'frustrated' by finite bandwidth effects in a predictable manner. We test our predictions by varying the differential character of the nonlinear terms in the model and excellent agreement is found at low

Communicated by Anthony Bloch and Peter Constantin.

✉ Ryan Shìjié Dù
ryan_sjdu@nyu.edu

[1] Courant Institute of Mathematical Sciences, New York University, New York, USA

Published online: 14 July 2023

wave amplitudes in all cases. At high amplitude, however, one case exhibits a novel 'breakthrough' turbulent regime that has not been observed before and for which no theory presently exists. Finally, we discuss the observable implications of our findings for other systems featuring wave turbulence, including the important case of oceanic inertia–gravity waves, for which the admissible frequency range is bounded above and below, thus limiting the achievable size of an inertial range a priori.

Keywords Majda–McLaughlin–Tabak model · Zakharov–Kolmogorov spectra · Wave turbulence · Dispersive waves · Inertial range

Mathematics Subject Classification 76B15 · 76F99 · 76F65 · 35Q86

1 Introduction

Wave turbulence theory (WTT) for ensembles of weakly interacting waves was invented by Peierls in his pioneering work on heat conduction in crystals (Peierls 1929). Much of the later development of WTT in the 1960s centered on the study of surface waves (Hasselmann 1962, 1963; Zakharov 1968) and since then the theory has been applied to very many wave systems in physics, including important recent applications to budgets of internal wave activity in the ocean (McComas et al. 1977; Lvov et al. 2010, 2012; Dematteis and Lvov 2021; Dematteis et al. 2022), which are important for the long-term dynamics of the ocean (Whalen et al. 2020). The central object in WTT is the kinetic equation, which governs the evolution of a suitable statistical measure of wave activity $n_k(t) \geq 0$ as a function of wavenumber k and time t (e.g. Zakharov et al. (1992); Nazarenko (2011)). The main feature of the kinetic equation that has been utilized to date is the prediction of non-trivial steady states that exhibit power laws and are associated with a cascade of conserved quantities through the so-called inertial range, i.e., through the band of wavenumbers that is well separated from both the wave forcing scales and the wave dissipation scales. This is reminiscent of the famous Kolmogorov $k^{-5/3}$ power law in three-dimensional hydrodynamic turbulence (Frisch 1995) and the associated power law exponents (or slopes in a log-log plot) are called Zakharov–Kolmogorov (ZK) slopes.

The measurement of such power laws in experimental, observational, or numerical wave studies has been the main test of WTT in real settings. Of course, observing an inertial range power law is only possible under a number of restrictive assumptions, not least the assumption that the bandwidth of the inertial range is wide enough. In practice, this makes it very hard to obtain unequivocal evidence for or against the validity of WTT in a given situation. Naturally, high-resolution direct numerical simulations of nonlinear waves are playing an increasingly important role in this area. In this connection, the Majda–McLaughlin–Tabak (MMT) model was proposed in Majda et al. (1997) (MMT97 hereafter) as a convenient one-dimensional toy model in which to explore the predictions of WTT. The restriction to one spatial dimension allows simulations with very high spectral bandwidth (two-dimensional versions of the MMT model have also been simulated recently in Hrabski and Pan (2022)). Using the supercomputing capabilities of the time, MMT97 integrated their equation to a forced–dissipative stationary state and measured the resultant very clear power

laws. However, none of their many runs showed the ZK power law, which is surprising as their model satisfies all the basic requirements for a kinetic equation based on four-wave resonances. This produced a long-standing puzzle, with many proposed solutions. MMT97 themselves constructed a heuristic scaling theory for their observed slopes. Subsequently, Cai et al. (1999, 2001); Zakharov et al. (2001, 2004); Rumpf et al. (2009); and others explored further avenues to explain the differences by experimenting on both the focusing and defocusing MMT model (to be defined below). In some of these studies the ZK slopes were observed in freely decaying defocusing wave turbulence experiments, but never in forced–dissipative experiments. Most recently, Chibbaro et al. (2017) (hereafter CDLO17) speculated that different power laws might result from different amplitude levels in the system, with the ZK slopes accurate at low amplitude and the alternative slopes observed by MMT97 arising at higher amplitude.

Here we reconsider this problem with a new combination of theory and numerical experiments aimed at the forced–dissipative energy cascade in the defocusing MMT model, which is assumed to feature an inertial range power law $n_k \propto k^{-p} P^r$ with exponents p and r. Here P is the constant spectral flux of wave energy from forcing to dissipation wavenumbers. In WTT for four-wave interactions the value $r = 1/3$ is hard-wired into the theory and the ZK value for the exponent p then follows from the kinetic equation (Zakharov et al. 1992). Here we do not make this assumption and instead find a more general one-parameter family of pairs (p, r) that are compatible with self-similar cascades. This opens the way to accommodate more than one power law exponent, and both the ZK value and the alternative MMT value are members of that family. We follow up on this with very high-resolution numerical simulations to test our theoretical results and to explore the factors that ultimately control the spectral slopes. We vary the spectral locations of forcing and dissipation (infrared and ultraviolet), as well as the level of nonlinearity. This yields a systematic study of the less-than-unity non-dimensional parameters that collectively determine the dynamics, which are

$$\left(\frac{H_2}{H}, \frac{\omega_-}{\omega_F}, \frac{\omega_F}{\omega_+} \right). \tag{1}$$

Here $\omega_\pm$ are the wave frequencies at the ultraviolet or infrared dissipation wavenumbers, respectively, ω_F is the wave frequency at the forcing wavenumber, and H_2/H is the ratio of nonlinear energy to total energy (full details are given in Sect. 2). Idealized WTT corresponds to a subtle limiting process in which all three of these parameters go to zero, but they are of course nonzero in any practical application. The parameters contain information about the finite size of the spectral domain, which we shall find crucial for the prediction of spectral slopes. In essence, our results show that for the direct cascade the most important non-dimensional parameter is ω_F/ω_+, which is small when the inertial range bandwidth is large. The robust result is that the observed slope differs from the ZK value by an amount that is proportional to an order one factor times ω_F/ω_+, hence the observed slope is always steeper than the ZK prediction. The impact of the other parameters is weak in comparison. In particular, in contrast to the findings in CDLO17, we find no evidence for a systematic change in the slope due to the nonlinearity level of the system.

Our simulations explain previous results that were obtained at lower numerical resolution and they delineate the stringent requirements that are necessary to reach the idealized regime of WTT. In a nutshell, in order to get close to the ZK slope values the inertial range must be wide when measured by frequency separation, not by wavenumber separation. In the MMT model the linear wave frequency is proportional to the square root of the wavenumber, so the frequency separation is a much more stringent requirement than the wavenumber separation. Our simulations achieve a clean inertial range with 2 decades in wavenumber and hence 1 decade in frequency. Previous simulations typically achieved inertial ranges with a decade in wavenumber and therefore only a factor three in frequency, which is the reason why the ZK value was not observed. On the one hand this might make it look hopeless to obtain clean power law exponents close to the ZK values for simulations of multi-dimensional forced–dissipative surface waves, for instance. On the other hand, the clear linear trend with ω_F/ω_+ allows the robust deduction of the limiting slope values by Richardson extrapolation from a few simulations with different ω_F/ω_+, which could be very useful for numerical simulations.

To test the validity of our conclusions for other systems we performed additional simulations of the defocusing MMT model with a modified differential form of the nonlinear terms. At low wave amplitude these always replicated our earlier results, which indicates that they might be of general interest to WTT. Surprisingly, at high wave amplitude one of the modified cases exhibited a fundamental transition to a completely new and different turbulent regime, which is not compatible with the familiar notions of a turbulent inertial range. Understanding this new regime is the subject of further research.

This manuscript is organized as follows. Section 2 describes the MMT model and its elementary properties. The generalized symmetry group argument for inertial ranges is developed in Sect. 3 and the numerical methods are described in Sect. 4. Comprehensive numerical results are provided in Sect. 5 and further simulations with modified nonlinearity are included in Sect. 6. Some concluding remarks are offered in Sect. 7.

2 Governing Equation and Properties

The defocusing MMT model describes the evolution of a complex-valued wave function $\psi(x,t)$ in one space dimension via the Schrödinger-like equation

$$i\frac{\partial}{\partial t}\psi = \mathcal{L}^{\alpha}\psi + \mathcal{L}^{\beta/4}\left(\left|\mathcal{L}^{\beta/4}\psi\right|^2 \mathcal{L}^{\beta/4}\psi\right). \tag{2}$$

Here $\alpha, \beta \in \mathbb{R}$ are parameters and the pseudo-differential operators are defined by their action on Fourier modes such that

$$\mathcal{L}^{\alpha}\exp(ikx) = |k|^{\alpha}\exp(ikx). \tag{3}$$

If $\alpha = 2$ and $\beta = 0$ then (2) is the standard nonlinear Schrödinger equation. Following the naming convention of the nonlinear Schrödinger equation, we study the defocusing

version of the model; the focusing version has the sign of the nonlinear term reversed. Like the Schrödinger equation, the MMT model is symmetric under spatial reflections $x \to -x$ and under the combined action of time reversal $t \to -t$ and conjugation $\psi \to \psi^*$. The dispersion relation for linear plane waves $\psi = A\exp(i[kx - \omega t])$ is

$$\omega(k) = |k|^\alpha. \tag{4}$$

Actually, a *single* plane wave is also an exact nonlinear solution, with amplitude-dependent frequency $\omega = |k|^\alpha + |A|^2|k|^\beta$. Broadly speaking, depending on its sign, the parameter β strengthens or weakens the nonlinearity at small scales.[1] The cubic nonlinearity implies that a mode with wavenumber k interacts with three other modes if

$$k_1 + k_2 = k_3 + k. \tag{5}$$

The standard four-wave WTT for this system is based on the existence of resonant quartets, i.e., sets of four wavenumbers for which (5) holds as well as

$$\omega(k_1) + \omega(k_2) = \omega(k_3) + \omega(k). \tag{6}$$

In particular, this holds if $\alpha = 1/2$, which replicates the dispersion relation of deep-water waves. We use periodic boundary conditions in a finite domain $x \in [0, L]$, which makes $\mathcal{L}^a$ a self-adjoint operator with respect to the standard inner product. We also have the group property $\mathcal{L}^a\mathcal{L}^b = \mathcal{L}^{a+b}$ and the useful identity

$$\int_0^L (\mathcal{L}^a\psi_1^*)(\mathcal{L}^b\psi_2)\,\mathrm{d}x = \int_0^L (\mathcal{L}^c\psi_1^*)(\mathcal{L}^d\psi_2)\,\mathrm{d}x \tag{7}$$

whenever $a+b = c+d$ (the star denotes complex conjugation). We define the Fourier series as

$$\varphi_k(t) = \int_0^L \exp(-ikx)\psi(x,t)\,\mathrm{d}x \quad \text{and} \tag{8}$$

$$\psi(x,t) = \frac{1}{L}\sum_{k\in\mathbb{Z}_L} \varphi_k(t)\exp(ikx) \tag{9}$$

where $\mathbb{Z}_L = \mathbb{Z}\cdot 2\pi/L$. In all simulations we set $L = 2\pi$, so the wavenumbers are integers.

2.1 Conservation Laws

The MMT model in (2) is a canonical Hamiltonian system with Hamiltonian functional

$$H = H_1 + H_2 = \underbrace{\int_0^L \left|\mathcal{L}^{\alpha/2}\psi\right|^2 \mathrm{d}x}_{=H_1} + \underbrace{\frac{1}{2}\int_0^L \left|\mathcal{L}^{\beta/4}\psi\right|^4 \mathrm{d}x}_{=H_2}. \tag{10}$$

[1] Our β has the opposite sign of the β in MMT97.

(In the focusing version the sign of H_2 is reversed, hence H is not sign-definite.) The total energy $H = H_1 + H_2$ is exactly conserved and at small amplitude its linear part H_1 is approximately conserved, which is exploited in WTT. The Fourier expression for H_1 is

$$H_1 = \frac{1}{L} \sum_{k \in \mathbb{Z}_L} \omega(k) |\varphi_k|^2. \tag{11}$$

The MMT model also conserves the L^2-norm of ψ, so the total wave action

$$N = \int_0^L |\psi|^2 \, \mathrm{d}x = \frac{1}{L} \sum_{k \in \mathbb{Z}_L} |\varphi_k|^2 \tag{12}$$

is constant. A canonical momentum with density $\mathrm{Im}(\psi^* \psi_x)$ is also conserved, but it is not sign-definite and has zero expected value for reflection-symmetric ensembles of solutions, so we do not consider it further.

2.2 Scaling Symmetry Group

The MMT model has a one-parameter scaling symmetry group that we will exploit in Sect. 3 to constrain self-similar spectral power laws. Consider an MMT solution $\psi(x, t)$ and apply the scaling group

$$\psi \to a\psi, \quad x \to bx, \quad t \to ct \tag{13}$$

with positive (a, b, c) to define $(\tilde{x}, \tilde{t}) = (bx, ct)$ and $\tilde{\psi}(\tilde{x}, \tilde{t}) = a\psi(x, t) = a\psi(\tilde{x}/b, \tilde{t}/c)$. The chain rule then implies $\tilde{\psi}_{\tilde{t}} = (a/c)\psi_t$ and $\tilde{\mathcal{L}}^\alpha \tilde{\psi} = (a/b^\alpha)\mathcal{L}^\alpha \psi$, for example, and then we can rewrite the MMT equation in terms of the rescaled $\tilde{\psi}(\tilde{x}, \tilde{t})$. Demanding that $\tilde{\psi}(\tilde{x}, \tilde{t})$ again solves the MMT equation then yields the two conditions

$$c = b^\alpha \quad \text{and} \quad a^2 = b^{\beta - \alpha}. \tag{14}$$

Combining (13) and (14) means that any MMT solution $\psi(x, t)$ gives rise to a one-parameter group of scaled MMT solutions

$$\psi_b(x, t) = a\psi(x/b, t/c) = b^{\frac{\beta-\alpha}{2}} \psi(x/b, t/b^\alpha) \tag{15}$$

indexed by the spatial rescaling parameter $b > 0$. For example, by using $b = 2\pi/L$ a solution $\psi_L(x, t)$ on a periodic domain of size L can be mapped to a solution on a circle via

$$\psi_{2\pi}(x, t) = \left(\frac{2\pi}{L}\right)^{\frac{\beta-\alpha}{2}} \psi_L(x(L/2\pi), t(L/2\pi)^\alpha). \tag{16}$$

2.3 Forcing and Dissipation

We add forcing and dissipation to the MMT model to study the statistics of stationary turbulent states. Specifically, we force the system (2) at a few central wave numbers and induce significant dissipation at very small (infrared) and very large (ultraviolet) wavenumbers. This yields

$$i\frac{\partial}{\partial t}\psi = \mathcal{L}^{\alpha}\psi + \mathcal{L}^{\beta/4}\left(\left|\mathcal{L}^{\beta/4}\psi\right|^2\mathcal{L}^{\beta/4}\psi\right) - i\mathcal{D}\psi + \mathcal{F}. \tag{17}$$

The spectral dissipation operator $\mathcal{D}$ is the same as the one used in MMT97, namely

$$\mathcal{D}\exp(ikx) = (\nu_-|k|^{-8} + \nu_+|k|^8)\exp(ikx) \tag{18}$$

where (ν_-, ν_+) are tunable hypo- and hyper-viscosity parameters. We use stochastic forcing

$$\mathcal{F}(x,t) = \sum_{k\in\mathbb{Z}_L} F_k \exp(ikx)[\xi_1^k(t) + i\xi_2^k(t)]. \tag{19}$$

The forcing amplitudes $F_k \in \mathbb{R}$ are non-zero only for a small set of reflection-symmetric wavenumbers (i.e., $F_k = F_{-k}$). The $\xi_i^k(t)$ are independent white noise processes such that the standard relations

$$\mathbb{E}\xi_i^k = 0 \quad \text{and} \quad \mathbb{E}\xi_i^k(t_1)\xi_j^k(t_2) = \delta_{ij}\delta(t_1 - t_2) \tag{20}$$

hold for expected values denoted by $\mathbb{E}$. The advantage of (19-20) over the deterministic instability forcing used in MMT97 and elsewhere is that the expected action and energy input rates can be computed a priori. Specifically, if $\mathcal{D} = 0$ then

$$\mathbb{E}\left(\frac{1}{L}\frac{\mathrm{d}N}{\mathrm{d}t}\right) = Q = \sum_{k\in\mathbb{Z}_L} 2|F_k|^2 \quad \text{and} \tag{21}$$

$$\mathbb{E}\left(\frac{1}{L}\frac{\mathrm{d}H_1}{\mathrm{d}t}\right) = P = \sum_{k\in\mathbb{Z}_L} 2|F_k|^2\omega(k) = \omega_F Q \tag{22}$$

are the expected action/energy injection rates per unit time and unit length. Note that the rates P and Q are intensive quantities whilst the conserved N and H are extensive quantities, proportional to the domain size L. The ratio $\omega_F = P/Q$ is the effective wave frequency of the forcing.

Equilibrated states of (17) result in a stationary and homogeneous random function $\psi(x,t)$ described by the invariant measure of the system. We denote by $\overline{(\cdot)}$ the mean value with respect to that invariant measure. In principle, this is an ensemble mean, but in practice we make the ergodic assumption and estimate it from suitable time-averaging over a long simulation run (cf. Sect. 4.2 below). Of primary interest in wave

turbulence are the mean values of $|\varphi_k|^2$, so we define the one-sided spectral action density n_k for $k \geq 0$ as

$$n_k = \frac{1}{L}\left(\overline{|\varphi_k|^2} + \overline{|\varphi_{-k}|^2}\right) = \frac{2}{L}\overline{|\varphi_k|^2} \tag{23}$$

if $k > 0$, and as $n_0 = \overline{|\varphi_0|^2}/L$ for $k = 0$. This suffices for a reflection-symmetric invariant measure and $\overline{N} = \sum_{k\geq 0} n_k$ holds by construction.

2.4 Action and Energy Cascades

The free evolution of the MMT model conserves (12) while one with small amplitude approximately conserves (11). Because $\omega(k)$ is a monotonically increasing function of $|k|$, (linear) energy tends to flow to larger wavenumbers and action tends to flow to lower wavenumbers. In a forced–dissipative statistical equilibrium a standard argument then yields precise cascade predictions if the forcing and dissipation occur at specific frequencies ω_F and (ω_-, ω_+) where $\omega_- < \omega_F < \omega_+$ (Fjørtoft (1953), MMT97). Let Q_- and Q_+ be the expected action dissipation rates at (ω_-, ω_+) and define the corresponding energy dissipation rates $P_\pm$ by multiplication with the corresponding frequency. In statistical equilibrium the two budgets $Q = Q_+ + Q_-$ and $\omega_F Q = \omega_+ Q_+ + \omega_- Q_-$ then yield

$$\frac{Q_-}{Q} = \frac{\omega_+ - \omega_F}{\omega_+ - \omega_-} \quad \text{and} \quad \frac{Q_+}{Q} = \frac{\omega_F - \omega_-}{\omega_+ - \omega_-}. \tag{24}$$

If $\omega_- \ll \omega_F \ll \omega_+$ then most action flows to the infrared and most energy flows to the ultraviolet, i.e., $Q_- \approx Q$ and $P_+ \approx P$. In this regime the system has two well-defined inertial ranges that contain distinct turbulence cascades. Between the forcing and infrared dissipation, there is an *inverse cascade* where action flows to smaller wavenumbers; and between the forcing and ultraviolet dissipation, there is a *direct cascade* where (linear) energy flows to large wavenumbers.

Numerical simulations can only afford a finite range of wavenumbers and this is exacerbated by a concave dispersion relation such as $\omega = \sqrt{|k|}$ (i.e., $\alpha = 1/2$), which leads to an even smaller range of frequencies. This is why the simulations in MMT97 and Zakharov et al. (2004) had the forcing wavenumbers very close to the infrared dissipation wavenumbers. Similar issues arise in laboratory experiments in finite domains and with finite dissipation strength. To accommodate these situations, we only assume that $\omega_- \ll \omega_+$, but put no requirement on the position of ω_F (except that $\omega_- < \omega_F < \omega_+$). This leads to

$$\frac{Q_-}{Q} \approx 1 - \frac{\omega_F}{\omega_+} \quad \text{and} \quad \frac{P_+}{P} = \frac{\omega_+ Q_+}{\omega_F Q} \approx 1 - \frac{\omega_-}{\omega_F}. \tag{25}$$

Clearly, the frequency ratios are the dynamically relevant measures of the inertial range size rather than the corresponding wavenumber ratios. This means that the size

of the inertial range is in effect much smaller than suggested by the corresponding wavenumber ratio. We will return to this crucial point in Sect. 5.3 below.

3 Self-similar Inertial-Range Spectra

In a perfect inertial range it is assumed that neither the forcing nor the dissipation details matter, and hence the spectrum n_k is given by some universal function of k and the mean spectral flux of the respective cascading quantity, action in inverse cascade and energy in the direct cascade. With white-noise forcing these mean fluxes are known a priori to be equal to the expected input rates, i.e., $\overline{P} = P$ and $\overline{Q} = Q$. Hence in a perfect direct inertial range

$$n_k = f(k, P) \tag{26}$$

for some function $f(\cdot, \cdot)$ to be determined. Standard dimensional analysis applied to wave turbulence proceeds at this stage by assuming a power law between n_k and P based on the number of wave modes in a resonant set, e.g., $n_k \propto P^{1/3}$ for resonant quartets (Connaughton et al. 2003; Zakharov et al. 1992). We avoid this assumption and instead use the scaling symmetry of the MMT system from Sect. 2.2 to explore the implications of (26).

With each $\psi(x, t)$ in the averaging ensemble we can associate a rescaled solution $\tilde{\psi}(\tilde{x}, \tilde{t}) = a\psi(\tilde{x}/b, \tilde{t}/c)$. The rescaled ensemble average of solutions then presumably again satisfy (26), i.e.,

$$\tilde{n}_{\tilde{k}} = f(\tilde{k}, \tilde{P}) \tag{27}$$

holds with the *same* function f. This is the hallmark of a self-similar inertial-range spectrum. The validity of (27) for all $b > 0$ in (14) restricts the form of the function f. For this we need to work out the rescaling of n_k, k, and P. Evidently, $\tilde{L} = Lb$, $\tilde{k} = k/b$, and then $\tilde{\varphi}_{\tilde{k}} = ab\,\varphi_k$ follows from its definition in (8). Combining these yields $\tilde{n}_{\tilde{k}} = a^2 b\, n_k$. The rescaling of P is the the same as the rescaling of $\partial_t \omega(k)|\psi|^2$ and therefore $\tilde{P} = a^2 b^{-\alpha} c^{-1}\, P$. Combining these with (26) and (27) leads to

$$\tilde{n}_{\tilde{k}} = f(k/b, a^2 b^{-\alpha} c^{-1}\, P) \quad \text{and} \quad \tilde{n}_{\tilde{k}} = a^2 b\, n_k = a^2 b\, f(k, P). \tag{28}$$

Equating these two implies the functional restriction

$$a^2 b\, f(k, P) = f(k/b, a^2 b^{-\alpha} c^{-1}\, P) \quad \Rightarrow \quad b^{\beta-\alpha+1}\, f(k, P) = f(k/b, b^{\beta-3\alpha}\, P), \tag{29}$$

which holds for all $b > 0$.

3.1 Power Laws Based on Scaling Group

The general solution to (29) is given in Section A, but here we restrict to power laws

$$n_k = f(k, P) = C\, k^{-p} P^r. \tag{30}$$

Substituting (30) into (29) yields the condition

$$\text{SG energy:} \quad p(r) = 1 + \beta - \alpha + r(3\alpha - \beta). \tag{31}$$

This shows that self-similar power laws in the energy inertial range form a one-parameter family defined by this $p(r)$. Only in the special case $3\alpha = \beta$ is there a unique wavenumber power law exponent $p = 1 + 2\alpha$, regardless of r.

This derivation is readily repeated for the inverse action cascade by replacing P with Q, whose scaling follows from $\partial_t |\psi|^2$ as $\tilde{Q} = a^2 c^{-1} Q$. This yields the functional restriction

$$b^{\beta-\alpha+1}\, g(k, Q) = g(k/b, b^{\beta-2\alpha}\, Q) \tag{32}$$

for $n_k = g(k, Q)$. Power law solutions $g(k, Q) = Dk^{-p} Q^r$ are then possible if $p(r)$ satisfies

$$\text{SG action:} \quad p(r) = 1 + \beta - \alpha + r(2\alpha - \beta). \tag{33}$$

Here the special case $2\alpha = \beta$ has the unique exponent $p = 1 + \alpha$.

3.2 Comparison with Other Power Laws

Other power laws suggested for the MMT system are special cases of the self-similar spectra derived above. Most important are the Zakharov–Kolmogorov (ZK) spectra, which are the power law solutions to the wave kinetic equation. The ZK power law for the energy (direct) cascade in the MMT model is $n_k = C\, k^{-z} P^{1/3}$ with

$$\text{ZK energy:} \quad z = p(1/3) = 1 + \frac{2\beta}{3}, \tag{34}$$

and for the action (inverse) cascade it is $n_k = D\, k^{-z} Q^{1/3}$ with

$$\text{ZK action:} \quad z = p(1/3) = 1 + \frac{2\beta - \alpha}{3}. \tag{35}$$

In both cases the flux exponent is pinned to $r = 1/3$, which as mentioned before is generic for a kinetic equation based on resonant quartets. The integrand in such a kinetic equation scales as $O(n_k^3)$ and therefore the flux scalings $Q \propto n_k^3$ and $P \propto n_k^3$ are built-in and correspond to $r = 1/3$. The ZK exponents are a special case of the

SG exponents $p(r)$ for $r = 1/3$, i.e., $z = p(1/3)$. Not surprisingly, this confirms that the ZK spectra are consistent with self-similar solutions of the original equation.

Another reasonable value for the flux exponent is $r = 1/2$, which stems from the 'bare' MMT equation (2) before statistical averaging, in which the action flux scales as $O(|\psi|^4)$ by simple inspection of the nonlinear term. If this scaling survives under averaging then $Q \propto n_k^2$, or $r = 1/2$. It is characteristic for the kinetic equation that for small n_k its implied flux $Q \propto n_k^3$ is much weaker than the 'bare' flux $Q \propto n_k^2$. Setting $r = 1/2$ yields the exponents

$$\text{MMT energy:} \quad m = p(1/2) = 1 + \frac{\alpha + \beta}{2} \tag{36}$$

for the energy cascade $n_k = Ck^{-m} P^{1/2}$ and

$$\text{MMT action:} \quad m = p(1/2) = 1 + \frac{\beta}{2} \tag{37}$$

for the action cascade $n_k = Dk^{-m} Q^{1/2}$. Historically, the energy power law exponent (36) was observed in all the simulations reported in the original paper MMT97, so we refer to it as the MMT spectrum. It appears plausible that in practice the relevant range of the exponent r is between $1/3$ and $1/2$. As an aside, MMT97 also derived a new heuristic turbulence closure, which for $\alpha = 1/2$ agrees with the energy power law (36). However, for other values of α in the energy cascade, and for any value of α in the action cascade, this new closure is not compatible with the self-similar spectra derived here. Hence we will not consider their closure any further.

As mentioned before, CDLO17 speculated that the ZK spectrum appears at low wave amplitude and is replaced by the MMT spectrum at high wave amplitude. In the present framework this corresponds to a transition from $r = 1/3$ to $r = 1/2$ as the amplitude increases. However, as detailed below, we have found no evidence of such an amplitude-dependent transition.

4 Numerical Methods

Our pseudo-spectral numerical methods are similar to those in MMT97, except for the white-noise forcing and for our use of a different technique to estimate mean quantities. Care is taken to eliminate spectral aliasing effects and the mean fluxes of energy and action are continuously monitored throughout the runs and compared to theoretical predictions. This is illustrated with a test run that exhibits both cascades.

4.1 Time-Stepping Method

The Fourier coefficients $\varphi_k(t)$ evolve as

$$\frac{\mathrm{d}}{\mathrm{d}t}\varphi_k(t) = \boldsymbol{L}\varphi_k(t) + \boldsymbol{N}(t) + \boldsymbol{F}(t), \tag{38}$$

where $\boldsymbol{L}$ is the Fourier symbol of the linear operators in (17), $\boldsymbol{N}$ represents the cubic nonlinear term, and $\boldsymbol{F}$ is the stochastic forcing. For the deterministic part we use an Integrating Factor method with Runge–Kutta fourth-order time-stepping (IF-RK4), which treats the stiff linear part of the equation exactly and hence allows the use of large numerical timesteps (Milewski et al. 1999; Yang et al. 2021). For a timestep between t_n and $t_{n+1} = t_n + \Delta t$ the exact solution of (38) is

$$\varphi_k(t_{n+1}) = \exp[\boldsymbol{L}\Delta t]\left(\varphi_k(t_n) + \int_{t_n}^{t_{n+1}} \exp[-\boldsymbol{L}(\tau - t_n)]\,[\boldsymbol{N}(\tau) + \boldsymbol{F}(\tau)]\,\mathrm{d}\tau\right). \tag{39}$$

How to use Runge–Kutta methods to approximate the deterministic integrand in (39) is studied in detail in Yang et al. (2021) and shown there to be the best choice for our MMT model. It is convenient and fast to evaluate $\boldsymbol{N}$ in real space using the Fast Fourier Transform (FFT), thus making this algorithm pseudo-spectral. For the white noise forcing $\boldsymbol{F}$ in (39) we use the Euler–Maruyama scheme. Focusing only on the stochastic term this means the explicit update step

$$\varphi_k(t_{n+1}) = \exp[\boldsymbol{L}\Delta t]\left[\varphi_k(t_n) + F_k(\Delta W_1^k + i\,\Delta W_2^k)\right], \tag{40}$$

where the Wiener increments ΔW_i^k are Gaussian random variables such that

$$\mathbb{E}\Delta W_i^k = 0 \quad \text{and} \quad \mathbb{E}\Delta W_i^k \Delta W_j^k = \delta_{ij}\Delta t. \tag{41}$$

Thus, after the deterministic IF-RK4 step we add an additional $\exp[\boldsymbol{L}\Delta t]F_k(\Delta W_1^k + i\,\Delta W_2^k)$ to account for the forcing. Note that the phase rotation part of $\exp[\boldsymbol{L}\Delta t]$ has no effect since the complex Gaussian is isotropic. And when the forcing is far from the dissipation in wavenumber, the dissipation part of $\boldsymbol{L}$ is also negligible. However, we always implement this IF correction to the forcing to be consistent. Finally, we de-alias in space by adjusting the ultraviolet dissipation such that the action density is negligibly small at half the maximally resolved wavenumber, which is the de-aliasing requirement for the cubic nonlinearity in the MMT system (17). The IF-RK4 method does not impose an obvious a priori stability requirement on the time step Δt, so in practice we ensured that Δt was small enough such that the statistics were insensitive to any further reduction of it. This led to typical time steps of size $\Delta t \approx 10^{-3}$.

4.2 Exponential Moving Time Average

Statistical mean quantities such as n_k are commonly estimated by time-averaging over long simulation runs, usually after discarding some initial data to eliminate start-up transients. We implement the time average in a different way, namely by estimating the mean quantities from moving time averages with an exponential kernel. This has three distinct advantages. First, it does not require treating the initial data differently, so runs can easily be stopped and restarted even after changing some parameters. Second, there

is an adjustable parameter for the exponential decay rate and by varying this parameter one can gain some insight into the autocorrelation time of the fluctuations. And third, the exponential averaging can be implemented with a simple explicit time stepping method and without the need to store additional data from earlier times.

So, with any time series $X(t)$ in the simulation we associate the estimator

$$Y(t) = \gamma \int_0^t e^{-\gamma(t-s)} X(s)\, \mathrm{d}s \tag{42}$$

for $\overline{X}$. Here $\gamma > 0$ is a decay rate chosen such that $1/\gamma$ is much larger than the autocorrelation time of the fluctuations in $X(t)$. In our simulations $1/\gamma$ was thousands of time units. Clearly, $Y(t)$ is a weighted average of $X(t)$ and it 'forgets' data that is in the distant past. The estimator is implemented by time-stepping the equivalent ODE

$$\frac{\mathrm{d}}{\mathrm{d}t} Y(t) = -\gamma(Y(t) - X(t)). \tag{43}$$

Approximating $X(t)$ as constant $X(t_{n+1})$ over a time step Δt yields the simple explicit formula

$$Y(t_{n+1}) = Y(t_n) + (1 - e^{-\gamma \Delta t})(X(t_{n+1}) - Y(t_n)). \tag{44}$$

We calculate $(1 - e^{-\gamma \Delta t})$ at the beginning and this is the only explicit occurrence of γ.

4.3 Test Run

We illustrate the setup of the model and the extraction of statistical diagnostics with an MMT test run with $\alpha = 1/2$ and $\beta = 0$. The number of Fourier modes is 2^{17}, which means that the highest wavenumber magnitude is 2^{16} and the highest de-aliased wavenumber magnitude is $2^{15} = 32768$. Thus the usable spectral bandwidth spans about 4 decades in k and 2 decades in $\omega(k)$. The action density input rate (21) is $Q = 7.5 \times 10^{-3}$ and distributed evenly among the eight modes in the symmetric forcing wavenumber set $|k| \in [399, 402]$. The dissipation coefficients are $\nu_- = 250$ and $\nu_+ = 2.5 \times 10^{-37}$ in (18), and with these choices the infrared and ultraviolet dissipation operators become important at $k_- \approx 2$ and $k_+ \approx 25000$, respectively. We obtained these wavenumbers from the action dissipation budget to be introduced in Sect. 4.4. We start with $\psi(x, 0) = 0$ and run the system up to $t = 2 \times 10^4$, which is well beyond the start-up transients. For the diagnostics we measure the inverse cascade power law in the range $|k| \in [40, 133]$ and the direct cascade power law in $|k| \in [1300, 2600]$.

Figure 1a shows a snapshot of the real part of $\psi(x, t)$ at the final time. The solution looks turbulent and spatially homogeneous without any appearance of obvious coherent structures. The estimated action density n_k is depicted in the log-log plot in Fig. 1b and shows clean and straight lines in the inertial ranges, implying the existence of power laws. We diagnose these power laws by measuring the slope of n_k

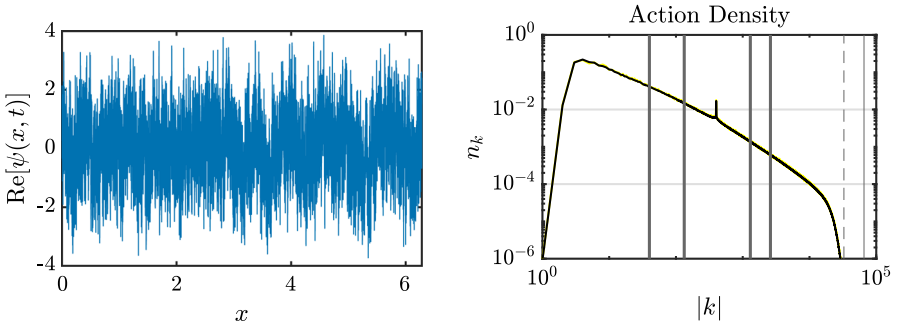

Fig. 1 **a** Snapshot of $\mathrm{Re}[\psi(x,t)]$ at the final time of the simulation ($t = 2 \times 10^4$). **b** Estimated action density n_k at the final time. Estimated power laws are $k^{-0.85}$ in the inverse cascade and $k^{-1.17}$ in the direct cascade. The thick vertical lines mark the inertial ranges in which we measure the power law slopes. The thin solid line is the maximum wavenumber in the numerical resolution and the dashed line is half of that, illustrating the usable de-aliased wavenumber range

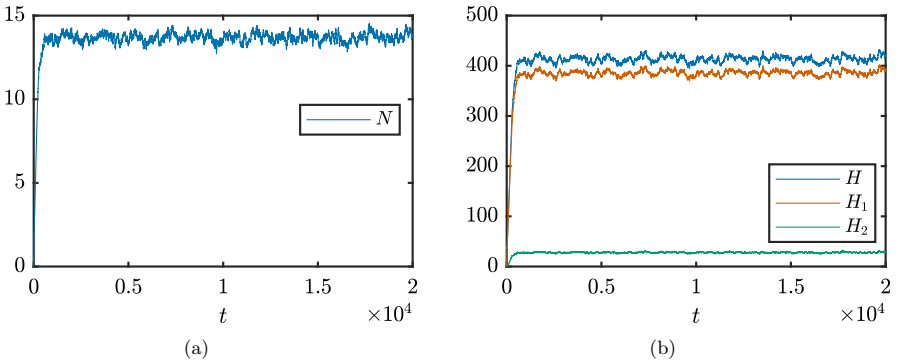

Fig. 2 **a** Time evolution of total action (N) in the simulation. **b** Same for the total energy (H), linear energy (H_1), and nonlinear energy (H_2) in the simulation. At the final time $H_2/H \approx 0.068$

in the log-log plot via linear least-squares, which produces $k^{-0.85}$ in the inverse cascade and $k^{-1.17}$ in the direct cascade. The plot also shows a reassuring decay of the action density towards the de-aliasing threshold. Figure 2 shows the time evolution of the instantaneous (N, H, H_1, H_2). After a short transient they oscillate around their constant means. H_2/H is small, so presumably this run is in the weakly nonlinear regime.

From $n_k \propto P^r$ or $n_k \propto Q^r$ we can diagnose the flux-related exponent r in the two cascades. To do this we change the forcing amplitude (and hence P and Q) and average the action density over the inertial range measurement windows used previously. Figure 3 shows log-log plots between the averaged n_k and the forcing inputs and the best fit straight line whose slope is the numerically measured r. The measured $r \approx 0.38$ in both cascades, which is in the 'reasonable' range $r \in [0.33, 0.5]$ that we expected from the argument in Sect. 3.2. The value of r is quite close to the

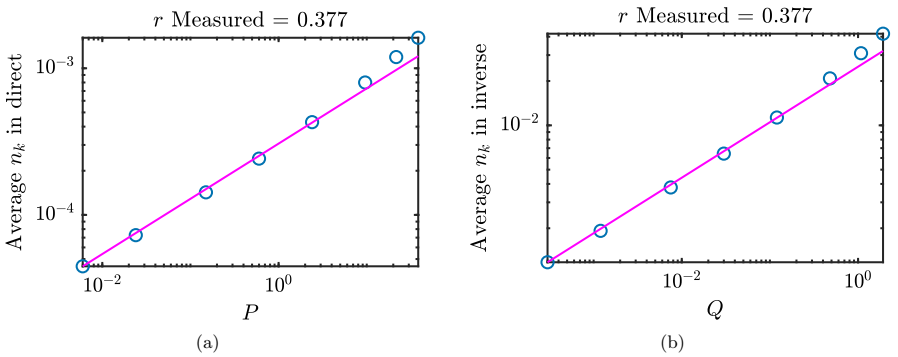

Fig. 3 The log-log plot between typical values of n_k (diagnosed from taking the average of n_k in the inertial ranges) and values of **a** action input P and **b** linear energy input Q. The magenta line is the linear fit over the first five data points. Their slopes are recorded in the titles as measured r

Table 1 Theoretical and observed power law exponents in the inverse and direct cascades

	z	m	Observed p	Observed r	SG $r = 0.38$
Action (inverse) cascade	0.83	1	**0.85**	**0.38**	0.88
Energy (direct) cascade	1	1.25	**1.17**	**0.38**	1.07

The first column is the Zakharov–Kolmogorov prediction $z = p(1/3)$ and the second column gives the MMT alternative $m = p(1/2)$. The two next columns (in bold) show observed values. The final column is the self-similar exponent $p(r)$ computed using the observed value $r \approx 0.38$ from the runs

0.33 assumed in the kinetic equation, but the difference is statistically significant. This is a typical result in our simulations.

Table 1 summarizes the test results and compares the observed slopes to the various theoretical slopes discussed in Sects. 3.1–3.2. The ZK prediction in the first column is the best fit in the inverse cascade but not in the direct cascade, and the opposite is true for the MMT prediction in the second column. The self-similar prediction for p in the final column is based on the measured value of r, and this gives the best overall fit in both cascades.

4.4 Flux and Dissipation Diagnostics

From the governing equation (38) we can diagnose the action dissipation as well as the spectral transport of action due to the nonlinear terms. The instantaneous contribution of the dissipation operator (18) to $\partial_t |\varphi_k|^2/L$ at each wavenumber is

$$2(\nu_- |k|^{-8} + \nu_+ |k|^8)|\varphi_k|^2/L, \tag{45}$$

so the mean value of this gives the net dissipation rate as a function of k. Similarly, if in (38) we denote the value of $\boldsymbol{N}$ at wavenumber k by b_k then the instantaneous time

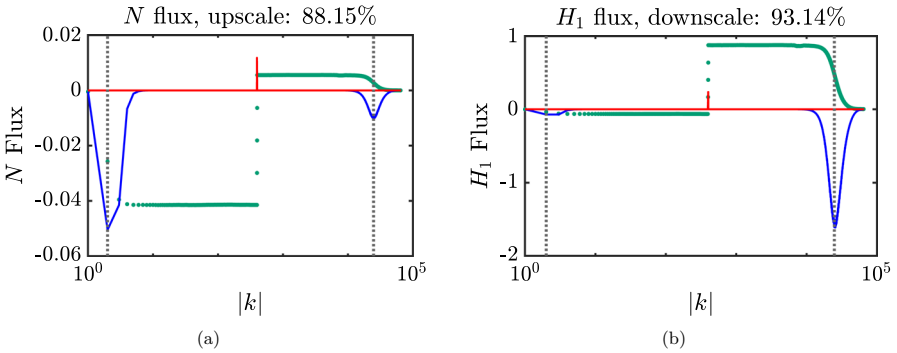

Fig. 4 Time tendency of **a** action (N) and **b** linear energy (H_1) by various terms of the equation. Red lines represent the forcing, blue lines dissipation, and green lines the flux due to the nonlinear term. (Note that the dissipation blue lines are plotted in 'area norm,' that is a multiplication by $|k|$, to make the dissipation at high wavenumbers visible.) Dotted vertical lines are the diagnosed location of dissipation. Numerically diagnosed percentages of **a** N that goes upscale and **b** H_1 that goes downscale are in the titles of the figures

tendency due to the nonlinear term is

$$(\varphi_k b_k^* + \varphi_k^* b_k)/L = 2\mathrm{Re}(\varphi_k b_k^*)/L \tag{46}$$

where star means complex conjugate. To diagnose the nonlinear spectral action transport from this we utilize the global conservation of action when summed over all k. Hence we sum (46) over the wavenumber band $k \in [-K, K]$ with $K > 0$. By global conservation, this must be equal and opposite to the sum over all the wavenumbers outside this band, and therefore this sum is equal to minus the nonlinear transfer of action across $|k| = K$. This is a spectral flux but no assumption of locality is made here. The same can be done for the flux of linear energy H_1 by multiplying (46) with $\omega(k)$. Notably, these instantaneous flux values are extremely noisy, with fluctuations that exceed their mean values by several orders of magnitude, so time-averaging is crucial here.

Figure 4 shows the spectral action and energy tendencies by the various terms. The forcing (represented by red lines) is zero except at a few central wavenumbers. The dissipation (represented by blue lines) is only significant at small and large wavenumbers. We use the strongest dissipation densities to define the dissipation wavenumbers k_- and k_+ and calculate ω_- and ω_+ from (4). The N and H_1 flux due to the nonlinear term (represented by green lines) shows both upscale and downscale flux, while most N goes upscale and most H_1 goes downscale. We use the value of action density fluxes at the left and right of the forcing, sufficiently far from the effect of dissipation, to calculate the percentage of action flowing upscale (Q_-/Q) and similarly for P_+/P. This provide us with a means to verify the relation (25). For our example, we calculate from (25), using the measured ω's, that

$$\frac{Q_-}{Q} \approx 1 - \frac{\omega_F}{\omega_+} = 0.8730 \quad \text{and} \quad \frac{P_+}{P} \approx 1 - \frac{\omega_-}{\omega_F} = 0.9293. \tag{47}$$

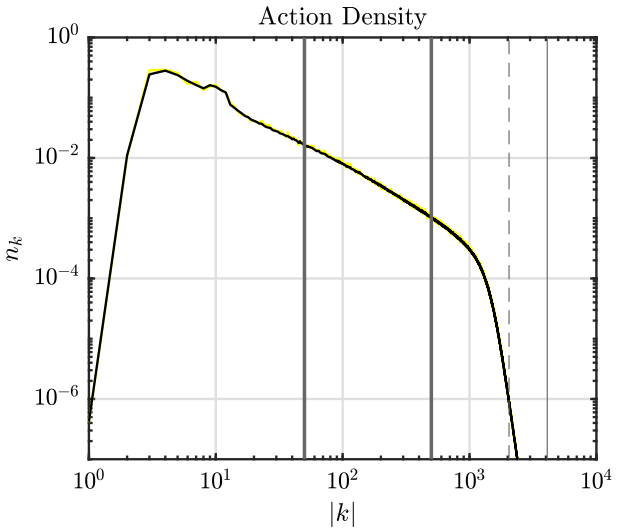

Fig. 5 Action density spectrum of a run that resembles the $\beta = 0$ case in Fig. 14d of MMT97. The vertical lines represents the same quantities as the ones in Fig. 1b. In particular, we have chosen the inertial range to be $|k| \in [50, 500]$ following MMT97. The direct cascade spectrum slope is 1.245 and $H_2/H \approx 0.0839$

These are very close to the diagnosed values in the titles of Fig. 4. So (25) works well.

4.5 Compare with Results from MMT97

Finally, to anchor our numerical results in precedent, we replicated the numerical results for the $\beta = 0$ case in MMT97. This comparison run used 2^{13} Fourier modes, as they did, which is 16 times fewer than in the Sect. 4.3 test run. The forcing is at $|k| \in [9, 12]$ and we set $\nu_+ = 1.0737 \times 10^{-27}$. Figure 5 shows the action density spectrum of the experiment, which is very close to the one shown in Fig. 14d of MMT97. The nonlinearity of the system is weak, with $H_2/H \approx 0.0839$. We measure the inertial range power law in $|k| \in [50, 500]$, again following MMT97, and obtain a slope of 1.245, which is again very close to the results from MMT97. The similarity of the results gives us confidence that our numerical algorithm works well and that the switch to white noise forcing did not change the relevant statistics. The new runs described below were run at much higher resolution, using up to 2^{19} modes.

5 Numerical Study of the Direct Cascade

We continue to use $\alpha = 1/2$ and $\beta = 0$ and now focus on the direct cascade, so for this purpose we move the forcing to lower wavenumbers in order to maximize the size of the direct inertial range. Our aim is to explore in detail the dependence of the power law exponents in $n_k = Ck^{-p}P^r$ on the three non-dimensional less-than-unity ratios in (1) that collectively determine the turbulent statistics of the MMT model with finite

inertial ranges. We find that the nonlinearity parameter H_2/H has only a weak impact on the power law exponent whilst the impact of the frequency parameter ω_F/ω_+ is very strong, but also takes a simple and very predictable form. This is a new result. The impact of the other frequency parameter ω_-/ω_F is noticeable but much less strong.

5.1 Setup for the Simulations

Values of H_2/H from close to zero up to one half (i.e., $H_1 = H_2$) are achieved by varying the energy flux P in (22) over four orders of magnitude. The total integration time and time step size are taken inversely proportional to the square root of the flux, since a more nonlinear system evolves faster and enters equilibrium faster. We have direct control over ω_F by selecting the forced wavenumbers and indirect control over the dissipation frequencies via the dissipation constants ν_- and ν_+ in (18). If in one numerical experiment ν_+ corresponds to dissipation at k_+ then we expect that $A^{-8}\nu_+$ corresponds to dissipation at Ak_+, roughly. A similar scaling holds for the infrared dissipation. We also scale ν_- and ν_+ proportional to the square root of the flux. We use this to prescribe the rough position of dissipation, but after each numerical experiment we diagnose of exact $\omega_\pm$ values using the methods described in Sect. 4.3.

5.2 Influence of Nonlinearity Parameter

The nonlinearity parameter H_2/H mediates between weak and strong turbulence, with the possibility of attendant changes in the spectral power laws. Specifically, for $\alpha = 1/2$ and $\beta = 0$, CDLO17 explored the hypothesis that the ZK power law k^{-1} is attained for weak turbulence $H_2 \ll H_1$ whilst the MMT law $k^{-1.25}$ is attained for strong turbulence $H_2 \sim H_1$. In terms of the self-similar spectra discussed earlier, this would correspond to a transition from $r = 1/3$ to $r = 1/2$, which appears plausible a priori. In CDLO17 this was explored using a large number of runs with varying H_2/H_1 and support for this hypothesis was found. However, these runs had a relatively limited spectral bandwidth with only 2^{13} modes (the same as in MMT97), so that the width of the direct inertial range was only about a decade in wavenumber and only a factor of about 3 in frequency.

To settle this we performed larger runs with 2^{17} modes forced at $|k| \in [99, 102]$, which allows for direct cascade inertial range of 2 decades in k and 1 decade in ω. Results are displayed in Fig. 6. The direct cascade slope does steepen as the nonlinearity increases, however, in contrast with the results in CDLO17, the change in slope is not very big, and the slope does not seem to range between 1 and 1.25. Note that this includes runs where the nonlinear energy is as large as the linear energy, indicating strong turbulence.

To resolve this discrepancy between our results and those in CDLO17, we replicated their simulations with our model (see "Appendix B" for details). This showed that the discrepancy was indeed due to the limited bandwidth of the earlier simulations. We also noticed that the slope results in CDLO17 were sensitive to the definition of the inertial range: measuring the slopes further from the forcing gave significantly different slopes from the ones reported in CDLO17.

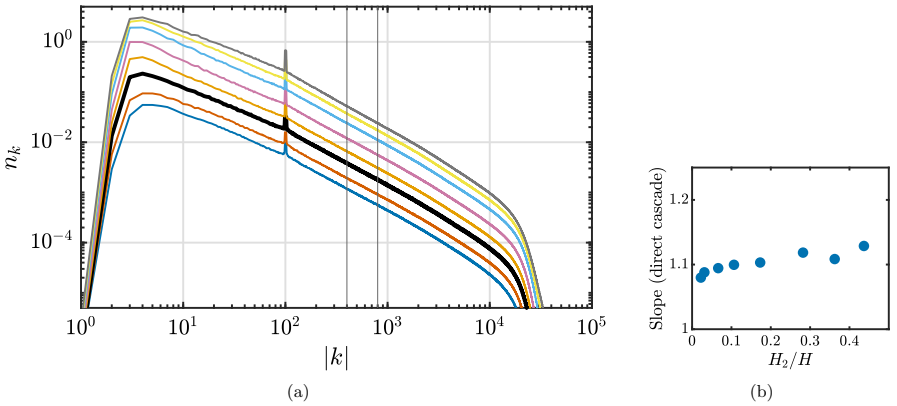

Fig. 6 MMT runs with 2^{17} modes to illustrate the effect of changes in H_2/H. The setup is similar to that in Sect. 4.3, expect forcing is near $|k| = 100$ and the magnitude of the forcing changes across different runs. **a** The action spectrum n_k. Its magnitude changes strongly with the forcing, but its slope changes only moderately. The experiment marked with thicker black line is the same as the one marked with the same style in Fig. 7. **b** The measured direct cascade slope as a function of H_2/H

Overall, our conclusions here are that the influence of the nonlinearity parameter H_2/H on the MMT dynamics is modest and that it certainly does not explain the disagreement between the numerical results of MMT97 and the predictions from wave turbulence theory.

5.3 Influence of Frequency Ratios

The ratio $\omega_F/\omega_+ \leq 1$ measures the frequency bandwidth of the energy inertial range, with smaller values corresponding to a larger bandwidth. It turns out that this parameter exerts a surprisingly strong influence on the observed power law, even if the inertial wavenumber range appears well separated from the forcing and ultraviolet dissipation wavenumber locations. This is demonstrated in Fig. 7, which displays a sequence of runs with greatly increasing ω_+ facilitated by using up to $2^{19} = 524\,288$ Fourier modes. Clearly, as the bandwidth increases the direct cascade power law becomes shallower *across its entire range* between the forcing and the dissipation wavenumbers. Moreover, as ω_F/ω_+ becomes very small the slope converges to the ZK k^{-1} power law in (34), as predicted by wave turbulence theory based on the standard four-wave kinetic equation. This convergence can be made more quantitative: we found that the observed power law exponent differs by an amount proportional to ω_F/ω_+ from its limiting value. Because $\omega = \sqrt{|k|}$, making this frequency ratio small enough to get close to the ZK exponent requires a very large spectral domain, explaining why this limit has not been observed in previous studies of forced–dissipative MMT turbulence.

Compared to ω_F/ω_+, the influence of the other frequency parameter ω_-/ω_F on the direct inertial range power law is much weaker. We established this with a number of runs across a wide range of the parameters ω_-/ω_F and H_2/H. We first look at the cases with weak nonlinearity ($H_2/H < 0.1$). Figure 8a shows that ω_-/ω_F has some effect on the direct cascade slope, but it does not change the trend that as ω_F/ω_+ goes

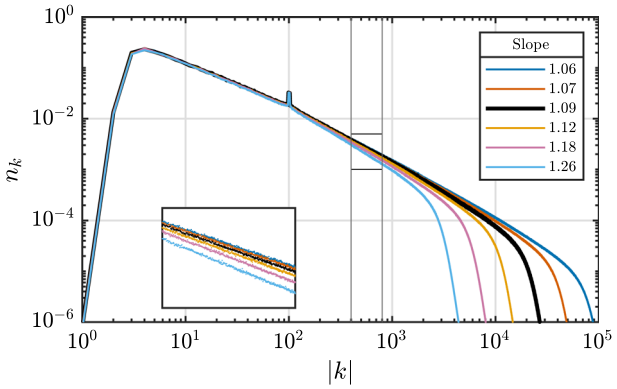

Fig. 7 Action density spectrum n_k versus ω_F/ω_+ with weak nonlinearity ($H_2/H < 0.1$). The ratio $\omega_-/\omega_F \approx 0.2$ is constant whilst the ratio ω_F/ω_+ changes from about 0.2 to 0.03 as the bandwidth increases. The experiment marked with thicker black line is the same as the one marked with the same style in Fig. 6a

to zero, the slope goes the ZK spectrum slope $z = 1$. This is even clearer in Fig. 8b. The parameter ω_-/ω_F influences the rate of change of the direct cascade slope with regard to ω_F/ω_+, but regardless of ω_-/ω_F, the slope tends to one as ω_F/ω_+ goes to zero. The final set of experiments, which is illustrated in Fig. 9, compares runs across a wide range of both the frequency ratios and the nonlinearity parameter H_2/H. We see that both ω_-/ω_F and H_2/H influence the direct cascade slope, but as ω_F/ω_+ tends to zero, the slope invariably tends to the ZK value $z = 1$. In these plots we also show the diagnosed r value using the method in Sect. 4.3. Interestingly, this diagnosed r value is quite stable across runs, hovering around $r \approx 0.4$. There is no clear convergence to $r = 1/3$, even though that value is expected to go hand-in-hand with the limiting value $z = 1$ from the kinetic theory based on four-wave resonances. We can synthesize our numerical results into the reasonably accurate empirical formula

$$n_k = C P^{0.4} k^{-p} \quad \text{with} \quad p \approx 1 + \frac{\omega_F}{\omega_+}\left(1.5 + 2\frac{\omega_-}{\omega_F} + 0.7\frac{H_2}{H}\right). \tag{48}$$

To first order in the small parameters $p - 1$ is proportional to ω_F/ω_+. A theoretical explanation for this formula is presently lacking.

6 Simulations with Nonzero β

Our simulations so far established a number of facts for the $\beta = 0$ MMT model: the spectral power law exponent in the direct cascade differed from the ZK limit by a significant amount proportional to ω_F/ω_+, the impact of the other frequency ratio ω_-/ω_F was much weaker, and the nonlinearity parameter H_2/H also had a weak impact and induced no systematic trend even at fairly high nonlinearity levels. A major question is now whether these facts carry over to other systems, thus allowing us to make testable a priori predictions in new situations.

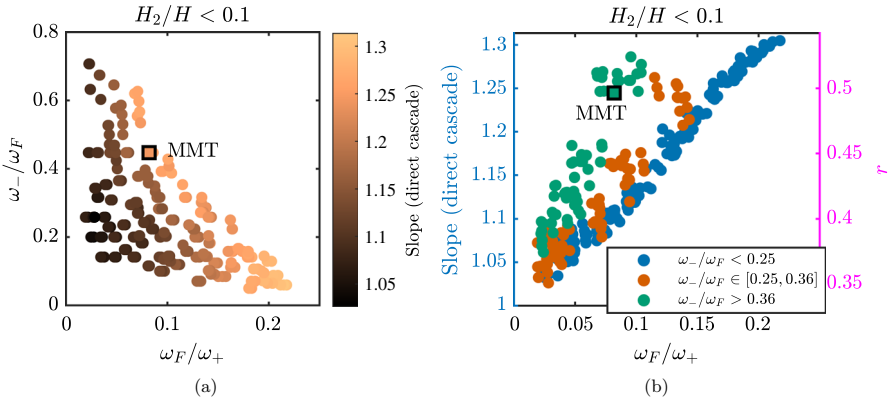

Fig. 8 Convergence of direct cascade slope for weak nonlinearity. The experiment in MMT97 that is reproduced in Fig. 5 is recorded with a square marked 'MMT.' **a** The slope is in color and ω_F/ω_+ and ω_-/ω_F are the x and y-axis; note the much larger scale on the y-axis. **b** Direct cascade slope versus ω_F/ω_+, with the three colors marking three groups of experiments with different values of ω_-/ω_F. The illustrative values of r on the right y-axis are computed from the observed slope p via (31)

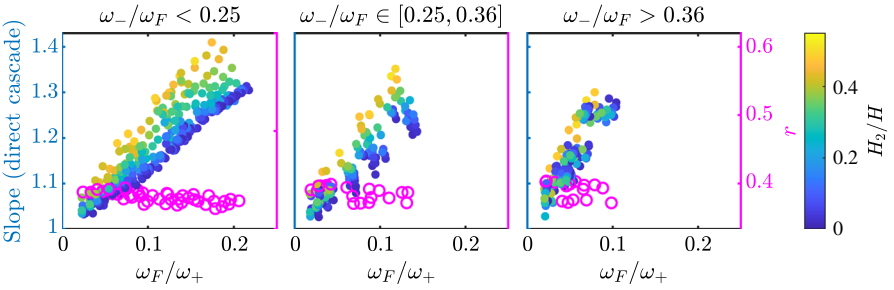

Fig. 9 Direct cascade slope with regard to ω_-/ω_F, ω_F/ω_+, and H_2/H. The sub-figures are grouped depending on the value of ω_-/ω_F (the same groups as the ones in Fig. 8b). The solid dots represent measures slopes, and the color is H_2/H. The magenta circles represent the diagnosed r value using the method in Sect. 4.3

Within the MMT model, we can explore this by running an additional suite of simulations with $\beta = \pm 1/3$, keeping $\alpha = 1/2$ fixed. Making the scale-selective nonlinearity parameter nonzero is certainly a substantial change in the model. The β parameter affects the scale-dependence of the nonlinear term such that $\beta > 0$ strengthens the nonlinearity at high wavenumbers and *vice versa* for $\beta < 0$. The ZK slopes for the direct cascade are

$$z = \frac{11}{9} \approx 1.22 \quad \text{and} \quad z = \frac{7}{9} \approx 0.77 \tag{49}$$

for $\beta = 1/3$ and $\beta = -1/3$, respectively. It turns out that the simulations follow our predictions closely for low nonlinearity levels, but then the $\beta = -1/3$ case also exhibited a completely new spectral 'breakthrough' regime at high nonlinearity, which changes the spectral shape completely and in a manner that is not compatible with

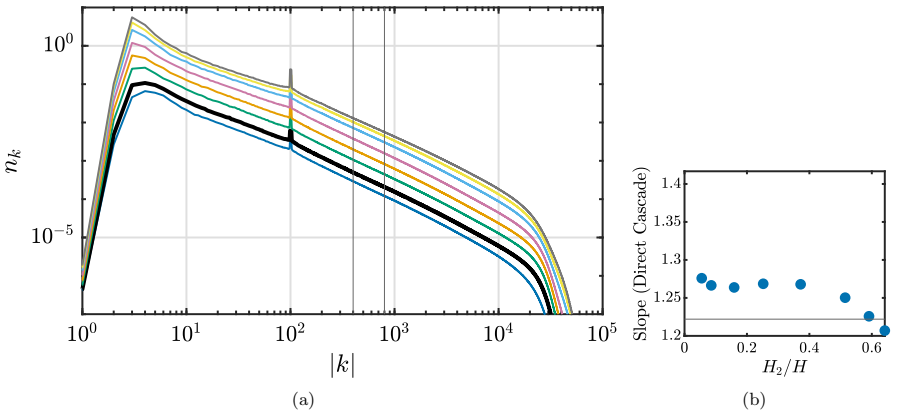

Fig. 10 **a** n_k for MMT model with $\beta = 1/3$ versus the the nonlinearity parameter H_2/H. The setup is the same as that of Fig. 6 and the experiment marked with thicker black line is the same as the one marked with the same style in Fig. 11. **b** The horizontal line marks the ZK slope $z \approx 1.22$

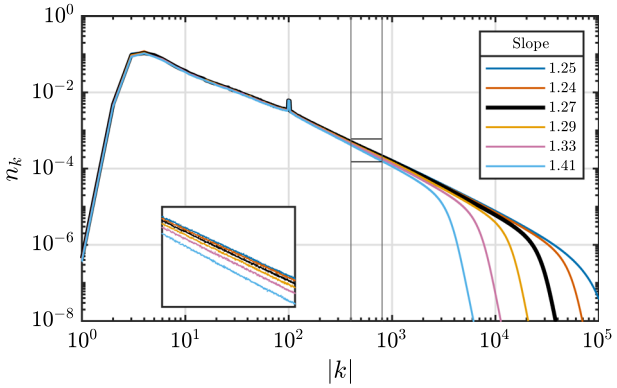

Fig. 11 n_k for MMT model with $\beta = 1/3$ versus the cascade bandwidth parameter ω_F/ω_+. The setup is the same as that of Fig. 7 and the experiment marked with thicker black line is the same as the one marked with the same style in Fig. 10. The nonlinearity is weak ($H_2/H < 0.1$)

familiar notions of forced–dissipative turbulence. The $\beta = +1/3$ case did not show such a new regime. We expect that this new highly nonlinear regime will require new theoretical tools to understand.

6.1 The $\beta = 1/3$ Case

We set $\beta = 1/3$ and explore the same scenarios as in Sect. 5. Figure 10 shows that the nonlinearity parameter (H_2/H) again only has a weak, non-systematic effect on the power law slope. At very large amplitude the slope now becomes shallower, but nothing else happens. Figure 11 shows that the frequency ratio ω_F/ω_+ also has the same strong impact as in the $\beta = 0$ case: the slope becomes significantly shallower as ω_F/ω_+ decreases and the cascade bandwidth increases. We summarize the quantitative

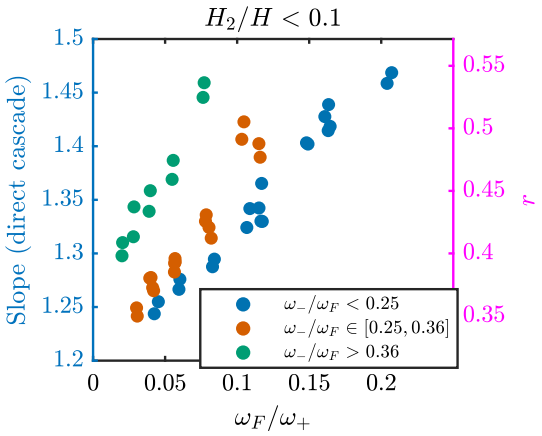

Fig. 12 Direct cascade slope versus ω_F/ω_+ for the MMT system with $\beta = 1/3$, similar to Fig. 8b. The ZK value is $z \approx 1.22$

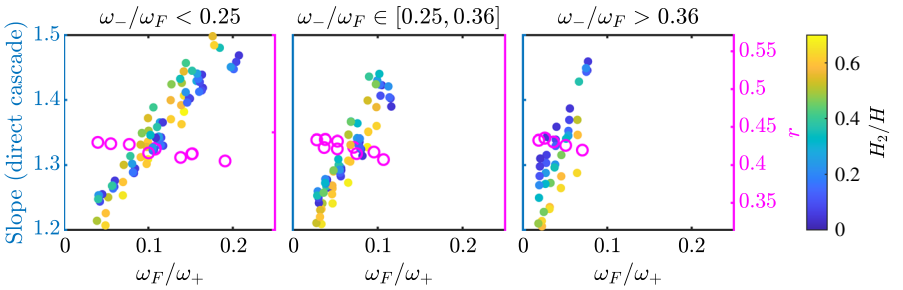

Fig. 13 Direct cascade slope versus ω_-/ω_F, ω_F/ω_+, and H_2/H for the $\beta = 1/3$ experiments, similar to Fig. 9

impact of all parameters in Figs. 12 and 13. Again, regardless of the ω_-/ω_F and H_2/H values, the slope converges to the ZK value as ω_F/ω_+ gets small. This corroborates the testable predictions from the $\beta = 0$ case, giving us confidence that there is some generality to our theoretical findings. Perhaps the strongest difference to the $\beta = 0$ case is that the directly measured r-values in the $n_k \propto k^{-p} P^r$ power law are now further away from the $r = 1/3$ value implied by kinetic theory.

6.2 The $\beta = -1/3$ Case

Figure 14 shows experiments with $\beta = -1/3$ with different nonlinearity H_2/H. The setup is similar to the experiments with $\beta = 0$ and $1/3$, except that we ran the experiment twice as long to ensure that all experiments have converged. Here we encounter a seemingly new turbulence phenomenon: for high nonlinearity there is a 'breakthrough' of the spectrum, i.e., a pile-up of energy at a wavenumber much larger than the forcing wavenumber k_F. In this regime it is no longer sensible to measure a spectral slope. The reason of this energy pile-up is unclear to us, but we have ruled out numerical errors by varying both resolution and time step without changing the result. We restricted to weaker nonlinearity in the remainder of our simulations

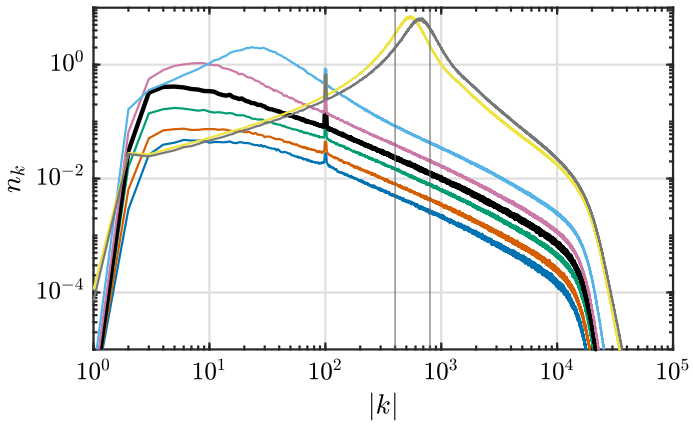

Fig. 14 n_k for MMT model with $\beta = -1/3$ versus H_2/H, showing a new highly nonlinear 'breakthrough' behavior and concomitant pile up of energy at high wavenumbers. The setup is the same as that of Fig. 6 and the experiment marked with thicker black line is the same as the one marked with the same style in Fig. 15

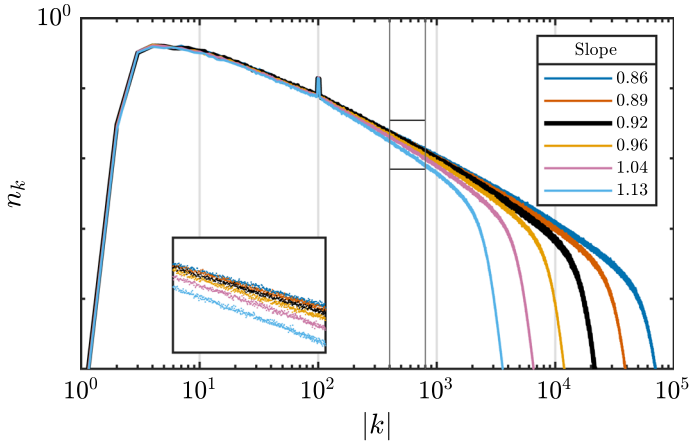

Fig. 15 n_k for MMT model with $\beta = -1/3$ versus ω_F/ω_+ at weak nonlinearity ($H_2/H < 0.1$). The setup is the same as that of Fig. 7 and the experiment marked with thicker black line is the same as the one marked with the same style in Fig. 14

($H_2/H < 0.1$). In Fig. 15 and 16 we see again that the slope converges to the ZK value as ω_F/ω_+ gets small. For these experiments the directly observed r-value was close to $1/3$ in all runs, which contrasts with the $\beta = 0$ and $\beta = 1/3$ cases.

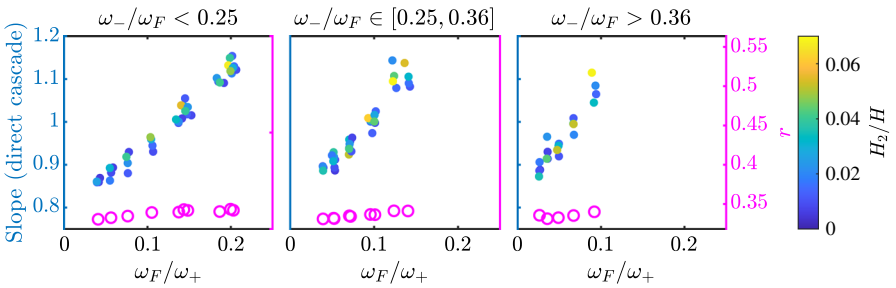

Fig. 16 Direct cascade slope with regard to ω_-/ω_F, ω_F/ω_+, and H_2/H, for the $\beta = -1/3$ experiments, similar to Fig. 9. Only Small H_2/H results are shown. The ZK value is $z \approx 0.77$ and the measured r-values are close to the $1/3$ from kinetic theory

7 Concluding Remarks

Our original expectation was that the different MMT spectra from previous numerical simulations could be explained as members of the one-parameter family of self-similar spectra $n_k \propto k^{-p} P^r$ that we derived in Sect. 3.1. This would also have been compatible with the hypothesis pursued in CDLO17. However, our high-resolution numerical simulations painted a different picture, in which the r-parameter is reasonably close to the WTT value $r = 1/3$ across the simulations, but the direct cascade wavenumber power law exponent p differs markedly from its WTT value $z = p(1/3)$ unless ω_F/ω_+ is very small (cf. (48)). Hence, the picture that actually emerges is that of an inertial range cascade that is 'frustrated' by the finite width of the inertial range as measured in the separation of the forcing frequency ω_F from the ultraviolet dissipation frequency ω_+. This finite spectral width breaks the self-similarity of the cascade and leads to the observed deviations from the ZK slopes.

For the inverse cascade some preliminary results suggest that, not surprisingly, the ratio ω_-/ω_F becomes the most important parameter. However, for a fixed size domain, there is a minimum value for k_- and hence ω_-, so this makes the direct and inverse cascade not entirely the same. Detailed investigation about the inverse cascade is outside the scope of the current paper.

There seems little doubt that the correct way to measure the width of the internal range in this context is by ω_F/ω_+ rather than by k_F/k_+, not least because of the simple linear appearance of the frequency ratio in (48). For a concave dispersion relation such as $\omega = \sqrt{|k|}$ the frequency bandwidth is much smaller than the wavenumber bandwidth, which is what limited earlier simulations in which the wavenumber bandwidth was about a decade, so the frequency bandwidth was only a factor of $3 - 4$. Only in simulations getting a frequency bandwidth of a decade or more could the ZK slope be directly observed. We could get close to this for the one-dimensional MMT system, but many practical applications are systems in two dimension or three. If they behave similarly as the MMT system, the requirement for spatial resolution gets unachievable quickly. However, not all hope is lost. We saw in Fig. 9 that the convergence to the ZK slope as $\omega_F/\omega_+ \to 0$ is rather linear, which means Richardson extrapolation from a few runs with different resolution would be successful.

In some applications of WTT the frequency bandwidth is bounded a priori, for example in the case of oceanic internal waves the frequency is bounded between the Coriolis frequency f and the buoyancy frequency N. In many oceanic regions, N/f is only about $30 - 50$, so a strong frequency separation is then impossible. If our conclusions about the necessity of a strong frequency separation for the inertial range carry over to these waves, then the predictions of WTT will inescapably be 'frustrated' by finite spectral width effects in these systems. Interestingly, the same is not true for pure sub-inertial waves in rotating unstratified systems, in which the buoyancy frequency $N = 0$ and the range of admissible wave frequencies now ranges from zero to f. This again allows for arbitrarily large frequency ratios and might make this case more amenable for the standard methods of WTT (cf. Monsalve et al. (2020) for recent experimental evidence in that direction).

A clear theoretical model for the simple impact of finite-width inertial ranges in WTT is currently missing. If the MMT system wave modes have significant non-local interactions, then the missing wave modes could perhaps explain the smaller value of the action density in the inertial range, and thus the steeper slope. Recent advances in wave turbulence theory for internal waves allow for estimating the relative importance of local and non-local wave interactions from integration of the wave-kinetic equation (Dematteis and Lvov 2021; Dematteis et al. 2022). It might be worthwhile to carry out similar calculations for the MMT system.

Finally, we note again that the amplitude dependence on our MMT turbulence states was surprisingly modest throughout, with the exception of the new 'breakthrough' high-amplitude phenomenon for the $\beta = -1/3$ model variant as described Sect. 6.2. We verified that this is not a numerical artifact, but any explanation or cogent description of this new phenomenon is currently lacking.

Acknowledgements We are grateful to Esteban Tabak for several interesting discussions of this project and for a draft of his original numerical scheme. This work was supported in part through the NYU IT High Performance Computing resources, services, and staff expertise. OB acknowledges financial support from ONR grant N00014-19-1-2407, NSF grant DMS-2108225, and from the Simons Collaboration on Wave Turbulence.

Author Contributions Both authors contributed to the study's conception, design, analysis, and writing of the manuscript. Data collection and visualization were performed by Ryan Shìjié Dù.

Data availability statement The code used in this manuscript is publicly available on Github: https://github.com/Empyreal092/MMT_Public.

Declaration

Conflict of interest I declare that the authors have no competing interests as defined by Springer, or other interests that might be perceived to influence the results and/or discussion reported in this paper.

Appendix A: General Self-similar Spectra Beyond Power Laws

The functional condition (29) allows solutions beyond power laws, which can be found by noting that (29) is a special case of the homogeneity relation

$$f(\lambda^{m_1}x, \lambda^{m_2}y) = \lambda^{m_3} f(x, y) \quad (\lambda > 0). \tag{50}$$

This has the general solution

$$f(x, y) = x^s y^t C(x^{m_2} y^{-m_1}) \tag{51}$$

provided the exponents are linked by

$$m_3 = m_1 s + m_2 t. \tag{52}$$

The $x^s y^t$ part of (51) is a power law family, but the second part now allows for an arbitrary function $C(\cdot)$ whose argument is invariant under the homogeneous scaling in (50).

To relate this to the direct energy cascade we set $\lambda = b$, $x = k$, $y = P$, $m_1 = -1$, $m_2 = \beta - 3\alpha$, $m_3 = \beta - \alpha + 1$, $s = -p$, and $t = r$. Hence the most general self-similar direct cascade spectrum is

$$n_k = k^{-p} P^r C(k^{\beta-3\alpha} P) \tag{53}$$

together with (31). (For the action cascade one finds the analogous result with an arbitrary function $D(k^{\beta-2\alpha} Q)$.) Even with an unknown function $C(\cdot)$ in place a peculiar power law can still be deduced if one were able to track n_k as a function of k along lines of constant $k^{\beta-3\alpha} P$ in (k, P) space, as then $C(\cdot)$ is constant and hence the unambiguous power law $n_k \propto k^{-1-\beta+\alpha}$ must hold along those lines. Of course, this requires comparing simulations over a sizable range of k and P.

Appendix B: Reproducing Results from CDLO17

We reproduced the runs in CDLO17 by greatly increasing ν_+ in order to reduce the spectral bandwidth. Also, CDLO17 used a rescaled MMT equation $i\phi_t = \epsilon_0^{-1} L\phi + |\phi|^2\phi$ with an explicit nonlinearity parameter ϵ_0. Their $\phi(x, t)$ can be mapped to our $\psi(x, t)$ via $\psi(x, t) = \sqrt{\epsilon_0}\phi(x, \epsilon_0 t)$. Figure 17a shows the action density based on $\psi(x, t)$ for a few experiments with different $\epsilon = H_2/H_1$, which is the parameter they used. The action spectra look very similar to Fig. 2 of CDLO17, after rescaling by ϵ_0 to change from their $|\phi|^2$ to our $|\psi|^2$. The central result of CDLO17 is its Fig. 3, which we reproduce here in Fig. 17b. The green dots are slopes measured from $|k| \in [20, 100]$, the same as CDLO17, while the orange data are alternative slopes measured from $|k| \in [50, 150]$, a bit further away from the forcing. The green dots match well with Fig. 3 of CDLO17 up to $H_2/H_1 \approx 0.8$, which is the highest value reported there. However, after that the slope keeps on increasing with H_2/H_1, until

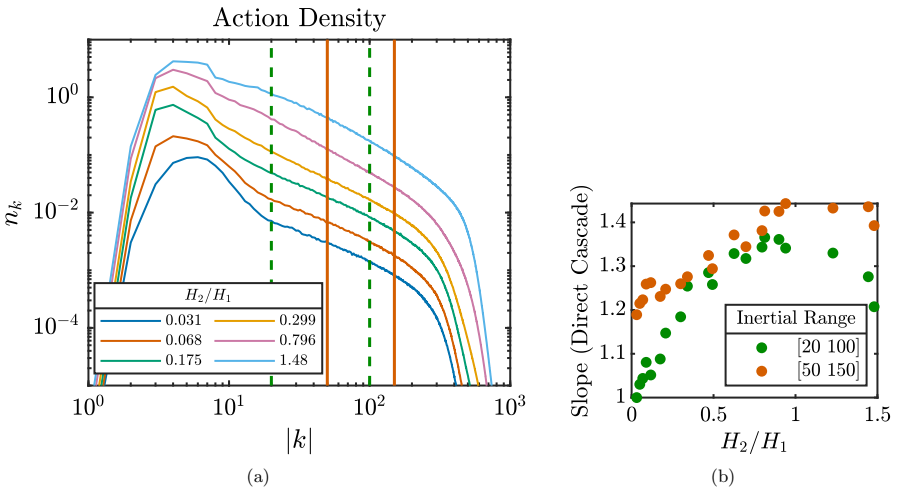

Fig. 17 A set of experiments to reproduce Fig. 2 and 3 of CDLO17. Forcing is at $|k| \in [4, 7]$, and $\nu_+ = 1.4074 \times 10^{-23}$ and $\nu_- = 50$ for the lowest H_2/H_1 cases, and scale as the increase in forcing. **a** A few example action density lines. The vertical lines mark the inertial ranges used in (**b**), which shows the slope versus H_2/H_1. Green dots are slopes measures from $|k| \in [20, 100]$ (the same as in CDLO17) and orange dots are from the alternative $|k| \in [50, 150]$

the trend reverses for $H_2/H_1 > 1$. Most importantly, these slope measurements are sensitive to the selection of inertial range. The orange data deviate much from the green dots even when H_2/H_1 is moderate. Note that when H_2/H_1 is small, the orange data actually has a slope of about 1.25, close to the result of MMT97. Overall, we concluded that the small spectral bandwidth of the experiments in CDLO17 does not allow robust extraction of spectral slopes in the inertial range.

References

Cai, D., Majda, A.J., McLaughlin, D.W., Tabak, E.G.: Spectral bifurcations in dispersive wave turbulence. Proc. Natl. Acad. Sci. **96**(25), 14216–14221 (1999). https://doi.org/10.1073/pnas.96.25.14216

Cai, D., Majda, A.J., McLaughlin, D.W., Tabak, E.G.: Dispersive wave turbulence in one dimension. Phys. D Nonlinear Phenom. **152**(153), 551–572 (2001). https://doi.org/10.1016/s0167-2789(01)00193-2

Chibbaro, S., De Lillo, F., Onorato, M.: Weak versus strong wave turbulence in the Majda–McLaughlin–Tabak model. Phys. Rev. Fluids **2**(5), 052603 (2017). https://doi.org/10.1103/physrevfluids.2.052603

Connaughton, C., Nazarenko, S., Newell, A.C.: Dimensional analysis and weak turbulence. Phys. D Nonlinear Phenom. **184**(1), 86–97 (2003). https://doi.org/10.1016/s0167-2789(03)00214-8

Dematteis, G., Lvov, Y.V.: Downscale energy fluxes in scale-invariant oceanic internal wave turbulence. J. Fluid Mech. **915**(A129), 1469–7645 (2021). https://doi.org/10.1017/jfm.2021.99

Dematteis, G., Polzin, K.L., Lvov, Y.V.: On the origins of the oceanic ultraviolet catastrophe. J. Phys. Oceanogr. **52**(4), 597–616 (2022). https://doi.org/10.1175/jpo-d-21-0121.1

Fjørtoft, R.: On the changes in the spectral distribution of kinetic energy for two dimensional, nondivergent flow. Tellus **5**(3), 225–230 (1953). https://doi.org/10.1111/j.2153-3490.1953.tb01051.x

Frisch, U.: Turbulence: The Legacy of A. N. Kolmogorov. Cambridge University Press, Cambridge (1995). https://doi.org/10.1017/CBO9781139170666

Hasselmann, K.: On the non-linear energy transfer in a gravity-wave spectrum part 1. General theory. J. Fluid Mech. **12**(4), 481–500 (1962). https://doi.org/10.1017/s0022112062000373

Hasselmann, K.: On the non-linear energy transfer in a gravity wave spectrum part 2. Conservation theorems; wave-particle analogy; irrevesibility. J. Fluid Mech. **15**(2), 273–281 (1963). https://doi.org/10.1017/s0022112063000239

Hrabski, A., Pan, Y.: On the properties of energy flux in wave turbulence. J. Fluid Mech. **936**(A47), 1469–7645 (2022). https://doi.org/10.1017/jfm.2022.106

Lvov, Y.V., Polzin, K.L., Tabak, E.G., Yokoyama, N.: Oceanic internal-wave field: theory of scale-invariant spectra. J. Phys. Oceanogr. **40**(12), 2605–2623 (2010). https://doi.org/10.1175/2010jpo4132.1

Lvov, Y.V., Polzin, K.L., Yokoyama, N.: Resonant and near-resonant internal wave interactions. J. Phys. Oceanogr. **42**(5), 669–691 (2012). https://doi.org/10.1175/2011jpo4129.1

Majda, A.J., McLaughlin, D.W., Tabak, E.G.: A one-dimensional model for dispersive wave turbulence. J. Nonlinear Sci. **6**, 9–44 (1997). https://doi.org/10.1007/BF02679124

McComas, C.H., Bretherton, F.P.: Resonant interaction of oceanic internal waves. J. Geophys. Res. (1896–1977) **82**(9), 1397–1412 (1977). https://doi.org/10.1029/jc082i009p01397

Milewski, P.A., Tabak, E.G.: A pseudo spectral procedure for the solution of nonlinear wave equations with examples from free-surface flows. SIAM J. Sci. Comput. **21**(3), 1102–1114 (1999). https://doi.org/10.1137/s1064827597321532

Monsalve, E., Brunet, M., Gallet, B., Cortet, P.-P.: Quantitative experimental observation of weak inertial-wave turbulence. Phys. Rev. Lett. **125**(25), 254502 (2020). https://doi.org/10.1103/physrevlett.125.254502

Nazarenko, S.: Wave Turbulence. Lecture Notes in Physics, vol. 825. Springer, Berlin (2011). https://doi.org/10.1007/978-3-642-15942-8

Peierls, R.: Zur Kinetischen Theorie Der Wärmeleitung in Kristallen. Annalen der Physik **395**(8), 1055–1101 (1929). https://doi.org/10.1002/andp.19293950803

Rumpf, B., Newell, A.C., Zakharov, V.E.: Turbulent transfer of energy by radiating pulses. Phys. Rev. Lett. **103**(7), 074502 (2009). https://doi.org/10.1103/physrevlett.103.074502

Whalen, C.B., De Lavergne, C., Naveira Garabato, A.C., Klymak, J.M., MacKinnon, J.A., Sheen, K.L.: Internal wave-driven mixing: governing processes and consequences for climate. Nat. Rev. Earth Environ. **1**(11), 606–621 (2020). https://doi.org/10.1038/s43017-020-0097-z

Yang, L.M., Grooms, I., Julien, K.A.: The fidelity of exponential and IMEX integrators for wave turbulence: introduction of a new near-minimax integrating factor scheme. J. Comput. Phys. **434**, 109992 (2021). https://doi.org/10.1016/j.jcp.2020.109992

Zakharov, V.E.: Stability of periodic waves of finite amplitude on the surface of a deep fluid. J. Appl. Mech. Tech. Phys. **9**(2), 190–194 (1968). https://doi.org/10.1007/bf00913182

Zakharov, V.E., Lvov, V.S., Falkovich, G.: Kolmogorov spectra of turbulence I. In: Calogero, F., Fuchssteiner, B., Rowlands, G., Segur, H., Wadati, M., Zakharov, V.E. (eds.) Springer Series in Nonlinear Dynamics. Springer, Berlin (1992). https://doi.org/10.1007/978-3-642-50052-7

Zakharov, V.E., Guyenne, P., Pushkarev, A.N., Dias, F.: Wave turbulence in one-dimensional models. Phys. D Nonlinear Phenom. **152**(153), 573–619 (2001). https://doi.org/10.1016/s0167-2789(01)00194-4

Zakharov, V.E., Dias, F., Pushkarev, A.: One-dimensional wave turbulence. Phys. Rep. **398**(1), 1–65 (2004). https://doi.org/10.1016/j.physrep.2004.04.002